Mechanics of Advanced Composite Structures 11 (2024) 203 – 216
This is an Open Access paper licensed under the Creative Commons License CC-BY 4.0 license.

Semnan University

Mechanics of Advanced Composite Structures

journal homepage: https://MACS.journals.semnan.ac.ir

Dynamic and Buckling Analysis of Hybrid Composite Beam Strengthened with Carbon Fibers/Aramid Fibers under Temperature Gradient

F. Basati , M.H.Yas *

Department of Mechanical Engineering, Razi University, Kermanshah, P.O.67346-67149, Iran

KEYWORDS

Carbon fiber;

Aramid fiber;

Hybrid ratio;

Buckling load;

Vibration.

ABSTRACT

Dynamic and buckling of a composite beam reinforced with a combination of carbon and aramid fibers is studied in this paper. The beam is under a thermal gradient through the thickness. Timoshenko beam is made of a polymer matrix (epoxy resin) reinforced with layers of high–strength carbon and high-toughness aramid fibers in order to create a balance between stiffness and toughness and create a type of structural composite beam with excellent strength and toughness. The mechanical and thermal properties of the hybrid composite beams are obtained based on the mixed law method. The equations of motion are extracted based on the Hamilton principle and then solved by the generalized differential quadrature method (GDQ). In this study, a thermal gradient is applied to the beam and then the vibration and buckling response of this hybrid composite beam are studied. The main contribution of this paper is the vibration and buckling responses of a hybrid composite structure strengthened by carbon and aramid fibers. The effect of the hybrid ratio as well as the stacking sequence on the free vibrations and critical buckling load are presented. The fundamental frequency and critical buckling load are largely affected by the stacking sequence. The conclusions show that the use of aramid fibers in the composite beam reinforced with carbon fibers decreases the natural frequency as well as the critical buckling load of the beam. The conclusions also show that for the symmetric hybrid composite beam, despite the critical buckling temperature being the same, the critical buckling load is different and depends on the location of the fibers.

1. Introduction

By examining research done on hybrid composite structures, it can be seen that these types of structures are very popular and used today compared to conventional composite structures due to their attractiveness and elimination of defects in their properties. The word 'aramid' is a contraction of 'aromatic polyamide'. Aramid fibers are organic materials used as reinforcement in composite structures with relatively low tensile modulus and strength. Aramid fibers are strong, with Young's modulus of 60 to 140 GPa. and a strength of 4.5 GPa in a gauge length of 2.5 cm with an elongation at a break of more than 4%. Aramid fibers can be used in different industries as follows [1]:

- In military industries such as making bulletproof vests
- Safety clothing and gloves.
- Sails for sailboats.
- Belts and hosing for industrial and automotive applications

* Corresponding author. Tel.: +98-0833433005
E-mail address: yas@razi.ac.ir

DOI: 10.22075/macs.2023.29813.1475
Received 2023-02-03; Received in revised form 2023-05-02; Accepted 2023-05-04.
© 2024 Published by Semnan University Press. All rights reserved.

- Aircraft body parts
- Electromechanical cables
- Friction linings such as clutch plates and brake plates
- Gaskets for great thermal and pressure applications
- Adhesives and sealants

Aramid fibers have better mechanical properties compared to steel and glass fibers in equal weight.

The characteristic of aramid fibers is that they are resistant to heat and flame and maintain this characteristic at high temperatures. Aramid fibers have been used commercially since the 1960s, first in the ballistic industry. The chemical structure of the aramid fibers is such that the bonds are aligned along the fiber axis and it provides extraordinary strength, flexibility, and wear resistance. The strong bond between the molecules causes the high strength of aramid fibers, also due to the high strength against heat and solvents, the fiber destruction temperature rises to 500°C. Aramid fiber has "inert" properties which provide a range of applications. However, aramid fibers are sensitive to ultraviolet (UV) light, acids, and certain salts [2-4]. Researchers experimentally presented the results obtained from tests to investigate the feasibility of strengthening multi-layered bamboo columns using aramid fiber-reinforced polymer composites (AFRP) and to investigate the effect of slenderness ratio on AFRP reinforced columns [5]. Polyamide-carbon fiber composites are lightweight and exhibit high strength, modulus, fatigue resistance, wear resistance, corrosion resistance, and higher electrical conductivity, along with impressive thermal, chemical inertness, and thermal stability properties [6]. Today hybrid composite material has grown a lot due to its lightness in the aerospace industry and is widely used in wings, cabin body, etc. [7-13]. Carbon fiber has an important role in making rocket engine shells, light vehicle equipment, sports equipment, and so on. However, this high resistance and modulus of carbon fibers cause great brittleness, low toughness, and low impact resistance in the composite [14-17]. Due to the lack of an energy-absorbing layer, external forces cause stress concentrate, which can overshadow the stability of the part. By using composite materials, the strengths of different reinforce can be combined and the weaknesses that exist in a composite material can be eliminated. Therefore, in order to eliminate the brittleness defect in the composite material, this defect can be eliminated by adding fibers that have high ductility and toughness [18-20].

Among the high-performance organic fibers that have high strength and toughness, we can mention polyethylene fibers that are used in the manufacture of bulletproof armor and protective clothing [21-22]. Polyimide fibers with great strength and great modulus, are a new kind of high-performance organic fiber. Apart from the good strength and toughness of polyimide fibers, this type of fiber has excellent resistance at high and low temperatures as well as ultraviolet rays and thermal stability [23-25]. Generally, polyimide fibers are known widely for their distinctive performance. Previous investigation has shown, the existence of polyimide fibers as reinforcement in polymer, causes strong surface adhesion of fibers with the resin matrix which increase the shear strength between the polyamide fibers with epoxy resin [26-27]. Cheon et al. presented the stab resistance mechanism and performance of the carbon, glass, and aramid fiber-reinforced polymer and hybrid composites [28]. They optimized the stacking sequence of a hybrid composite in order to modify the weakness of fiber-reinforced polymer. The mechanism of the stab resistance and the blade perforation for each fiber-reinforced polymer were investigated by static stab compressive tests. Currently, researchers considered the influence of aramid as well as carbon fibers with nanocarbon particles on the mechanical properties of EPDM rubber thermal insulators which can be used in solid rocket motors [29]. Kim et al. [30] evaluated carbon fiber and p-aramid composite for industrial helmets using simple cross-ply for protecting human heads. They studied mechanical properties such as impact absorption, tensile strength, bending strength as well as heat resistance.

Farokhian et al. presented the dynamic buckling of a smart sandwich nanotube. The nanostructure was composed of a carbon nanotube with inner and outer surfaces coated with ZnO piezoelectric layers, which play the role of sensor and actuator. Nanotube was under a magnetic field and the ZnO layers were under an electric field [31]. In further research in this field, vibration analysis in nanocomposite plates with smart layers was studied. The plate was reinforced by carbon nanotubes where the Mori-Tanaka law was utilized for obtaining the effective characteristic of structure assuming agglomeration effects [32]. Recently, the best lamination stacking sequences was predicted for the web and both flanges of cantilever double-tapered beam exposed to an externally uniformly distributed force to achieve the maximum lateral buckling capacity with optimized mass and material cost [33]. Soltani et al. used general differential quadrature as a powerful method to solve the governing equations for doing a comparative study on the lateral stability and strength of laminated composite and fiber metal

laminated I-shaped cross-section beams [34]. Soltani et al. studied Multi-objective optimization of lateral stability strength of transversely loaded laminated composite beams with varying I-section. They used classical lamination theory and Vlasov's model for thin-walled cross-sections [35]. A simple and novel method was presented for discussing the lateral-torsional stability of thin-walled symmetric balanced laminated beams with varying I-section. The method is based on the classic lamination theory and Vlasov's model [36]. Aydin et al. [37] studied comparative dynamic analysis of carbon, aramid, and glass fiber-reinforced interplay hybrid composites. Based on the experimental and numerical results, the effective factors in determining the natural frequency and damping ratio are lamina numbers, orientation angles, and fabric types. The novelty of this study is to find the right combination of the two types of fiber that might improve the brittleness of carbon fiber-reinforced polymer and at the same time be suitable for vibrations and buckling under temperature gradients. To the best of our knowledge, the vibration and buckling response of a hybrid composite structure strengthened by carbon fibers and aramid fiber has not been presented yet. Thus this work can be an inspiring reference for the design and material selection of structural composites.

2. Theory and Formulation

The composite beam consists of four layers of fibers with an epoxy matrix that includes carbon and aramid fibers. The mixed law is applied to obtain the mechanical and thermal properties of hybrid composites:

$$P_H = P_C V_C + P_P V_P \quad (1)$$

where P_H denotes the hybrid composite properties. P_C and P_P stand for carbon and aramid fibers respectively. V_C and V_P are volume percentages of carbon and aramid fibers respectively.

Fig. 1 shows the different arrangements of carbon and aramid fiber layers. As it is known, aramid fibers have high toughness and carbon fibers have high stiffness, and by combining them and making hybrid composites strengthened with carbon and aramid fibers (HFRP), the defects of the single-fiber composite are compensated.

In this study, we define hybrid ratio as follows:

$$Hybrid\ ratio = V_C/(V_C + V_P) \quad (2)$$

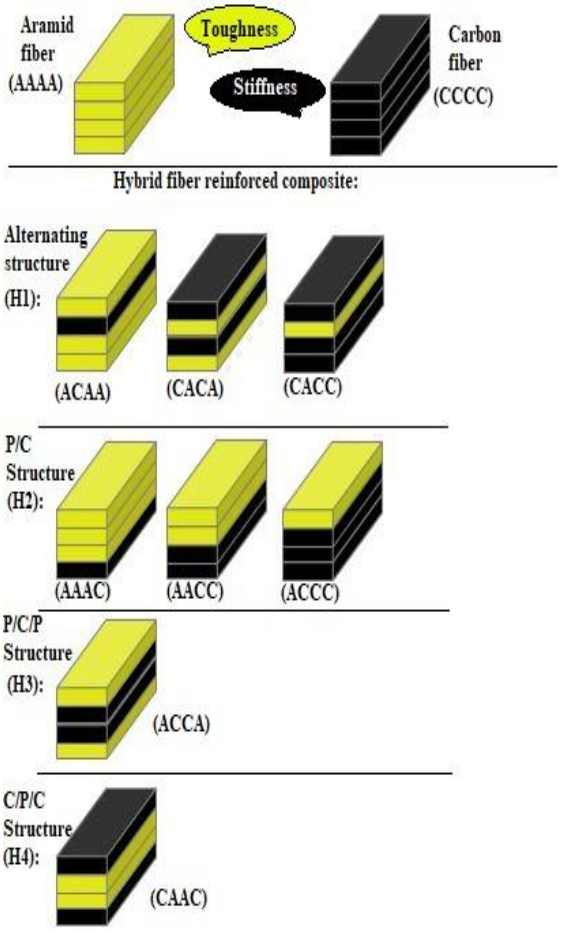

Fig. 1. Different arrangements of aramid and carbon fiber layers

The stacking sequence details of the hybrid composites with four layers are shown in Table 1. In this table, A and C symbols stand for carbon and aramid fibers respectively.

Fig.2 Shows the geometry of the composite laminated beam which is made of four layers of carbon and aramid fibers. It is assumed that the beam is under a thermal gradient $\Delta T(z)$ through the thickness direction. The temperature of the lower and upper surfaces is T_L and T_U respectively.

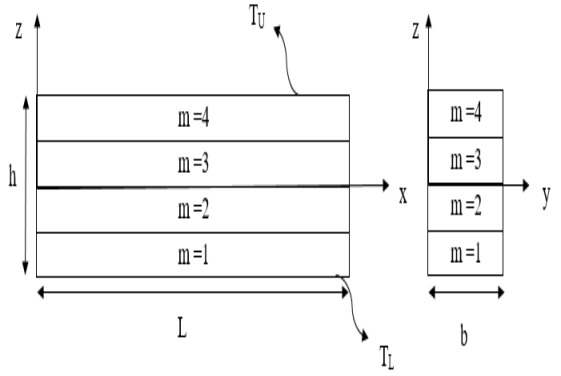

Fig. 2. Beam geometry

Table 1. Fiber arrangement of hybrid composites

Composite type		Layer number ratio (carbon/aramid)	Fiber arrangement	Hybrid ratio %
PFRP (Polymer fiber reinforced composite)		0/4	*AAAA*	0
CFRP (Carbon fiber reinforced composite)		4/4	*CCCC*	100
H1 Alternating composite beam	*H1-0*	1/3	*ACAA*	29
	H1-1-	2/2	*CACA*	55
H2 P/C composite beam	*H1-2*	3/1	*CACC*	79
	H2-1	1/3	*AAAC*	29
	H2-2	2/2	*AACC*	55
	H2-3	3/1	*ACCC*	79
H3 P/C/P composite beam (Symmetric stacking sequence)	*H3-1*	2/2	*ACCA*	55
H4 C/P/C composite beam (Symmetric stacking sequence)	*H4-1*	2/2	*CAAC*	55

The temperature distribution is obtained by solving the one-dimensional stable flow thermal conductivity equation:

$$-\frac{d}{dz}\left(k\frac{dT}{dz}\right)=0 \tag{3}$$

The thermal boundary conditions are as:

$$T(z)=T_L \qquad at\ z=-\frac{h}{2}$$

$$T(z)=T_U \qquad at\ z=\frac{h}{2} \tag{4a}$$

The continuity requirements at the interfaces:

$$T^{(1)}=T^{(2)} \qquad at \qquad z=-\frac{h}{4}$$

$$T^{(2)}=T^{(3)} \qquad at \qquad z=0 \tag{4b}$$

$$T^{(3)}=T^{(4)} \qquad at \qquad z=\frac{h}{4}$$

$$K^{(1)}\frac{dT}{dz}=K^{(2)}\frac{dT}{dz} \qquad z=-\frac{h}{4}$$

$$K^{(2)}\frac{dT}{dz}=K^{(3)}\frac{dT}{dz} \qquad z=0 \tag{4c}$$

$$K^{(3)}\frac{dT}{dz}=K^{(4)}\frac{dT}{dz} \qquad z=\frac{h}{4}$$

where the superscript shows the lamina number and *K* is the coefficient of thermal conductivity.

The distribution of the temperature field for each lamina is determined as follows:

$$T^{(m)}=a_1^{(m)}+a_2^{(m)}\int_{z_{m-1}}^{z}\frac{1}{K^{(m)}}dz, \quad m=1,2,3,4$$

$$a_1^{(1)}=T_L,\ a_2^{(1)}=a_2^{(2)}=a_2^{(3)}=a_2^{(4)}=\frac{(T_U-T_L)}{(t^{(1)}+t^{(2)}+t^{(3)}+t^{(4)})}$$

$$a_1^{(2)}=T_L+\frac{(T_U-T_L).t^{(1)}}{(t^{(1)}+t^{(2)}+t^{(3)}+t^{(4)})}$$

$$a_1^{(3)}=T_L+\frac{(T_U-T_L).(t^{(1)}+t^{(2)})}{(t^{(1)}+t^{(2)}+t^{(3)}+t^{(4)})}$$

$$a_1^{(4)}=T_L+\frac{(T_U-T_L).(t^{(1)}+t^{(2)}+t^{(3)})}{(t^{(1)}+t^{(2)}+t^{(3)}+t^{(4)})}$$

$$t^{(m)}=\int_{z_{m-1}}^{z}\frac{1}{K^{(m)}}dz, \qquad m=1,2,3,4 \tag{5}$$

where z_{m-1}, z_m shows the z-coordinate of the upper and lower faces of the *mth* lamina. To derive equations of motion, Timoshenko beam theory is utilized, which defines the displacement components as follows:

$$u(x,t) = u_0(x,t) + z\psi(x,t)$$

$$v(x,t) = 0 \tag{6}$$

$$w(x,t) = w_0(x,t)$$

u_0 and w_0 are displacement components in the middle face of the beam along the length and thickness of the beam, respectively, and ψ is the rotation angle around the y-axis. Hamilton principle is applied to derive the governing equations

$$\delta \int_0^t (T - \Pi + \Upsilon_p) = 0 \tag{7}$$

where T, Π and Υ_p are kinetic, elastic, and external potential energies respectively.

$$T = b/2(\int_0^L \int_{-h/2}^{h/2} \rho(z)((\frac{\partial u}{\partial x})^2 + (\frac{\partial u}{\partial t})^2)dzdx$$

$$\Pi = b/2(\int_0^L \int_{-h/2}^{h/2} (\sigma_{xx}\varepsilon_{xx} + \tau_{xy}\gamma_{xy})dz \tag{8}$$

$$\Upsilon_P = b/2(\int_0^L N_{x0}(\frac{\partial W}{\partial x})^2)dzdx$$

$$Q_{11}(z) = \frac{E(z)}{1-\upsilon^2} \quad , \quad Q_{55}(z) = \frac{E(z)}{2(1+\upsilon)}$$

$$N_{x0} = -\int_{-h/2}^{h/2} \alpha(z)Q_{11}(z)\Delta T(z),$$

By inserting Eq. (8) into Eq. (7), the governing equations are determined as follows:

$$A_{11}\frac{\partial^2 U}{\partial x^2} + B_{11}\frac{\partial^2 \Psi}{\partial x^2} + \frac{\partial A_{11}}{\partial x}\frac{\partial U}{\partial x} + \frac{\partial B_{11}}{\partial x}\frac{\partial \Psi}{\partial x} = I_0\frac{\partial^2 U}{\partial t^2} + I_1\frac{\partial^2 \Psi}{\partial t^2}$$

$$B_{11}\frac{\partial^2 U}{\partial x^2} + D_{11}\frac{\partial^2 \Psi}{\partial x^2} - k_s A_{55}\left(\frac{\partial W}{\partial x} + \Psi\right) + \frac{\partial B_{11}}{\partial x}\frac{\partial U}{\partial x} + \frac{\partial D_{11}}{\partial x}\frac{\partial \Psi}{\partial x} = I_1\frac{\partial^2 U}{\partial t^2} + I_2\frac{\partial^2 \Psi}{\partial t^2}$$

$$k_s A_{55}\left(\frac{\partial^2 W}{\partial x^2} + \frac{\partial \Psi}{\partial x}\right) + N_{x0}\frac{\partial^2 W}{\partial x^2} + k_s\frac{\partial A_{55}}{\partial x}\left(\frac{\partial W}{\partial x} + \Psi\right) + \frac{\partial N_{x0}}{\partial x}\frac{\partial W}{\partial x} = I_0\frac{\partial^2 W}{\partial t^2} \tag{9}$$

The governing equations in the dimensionless form are obtained as follows:

$$a_{11}\frac{\partial^2 \bar{U}}{\partial \xi^2} + b_{11}\frac{\partial^2 \Psi}{\partial \xi^2} + \frac{\partial a_{11}}{\partial \xi}\frac{\partial \bar{U}}{\partial \xi} + \frac{\partial b_{11}}{\partial \xi}\frac{\partial \Psi}{\partial \xi} = \bar{I}_0\frac{\partial^2 \bar{U}}{\partial \tau^2} + \bar{I}_1\frac{\partial^2 \Psi}{\partial \tau^2}$$

$$b_{11}\frac{\partial^2 \bar{U}}{\partial \xi^2} + d_{11}\frac{\partial^2 \Psi}{\partial \xi^2} - \eta a_{55}\left(\frac{\partial \bar{W}}{\partial \xi} + \eta\Psi\right) + \frac{\partial b_{11}}{\partial \xi}\frac{\partial \bar{U}}{\partial \xi} + \frac{\partial d_{11}}{\partial \xi}\frac{\partial \Psi}{\partial \xi} = \bar{I}_1\frac{\partial^2 \bar{U}}{\partial \tau^2} + \bar{I}_2\frac{\partial^2 \Psi}{\partial \tau^2}$$

$$a_{55}\frac{\partial^2 \bar{W}}{\partial \xi^2} + \frac{\partial}{\partial}(\bar{N}_{x0}\frac{\partial \bar{W}}{\partial \xi}) + \frac{\partial a_{55}}{\partial \xi}\frac{\partial \bar{W}}{\partial \xi} + a_{55}\frac{\partial \Psi}{\partial \xi} + \eta\frac{\partial a_{55}}{\partial \xi}\Psi = \bar{I}_0\frac{\partial^2 \bar{W}}{\partial \tau^2} \tag{10}$$

where the dimensional parameters are used as follows:

$$\xi = \frac{x}{L}, \overline{W} = \frac{W}{h}, \Psi = \varphi, \eta = \frac{L}{h}, \overline{U} = \frac{U}{h}$$

$$(a_{11}, a_{55}, b_{11}, d_{11}) = (\frac{A_{11}}{A_{11}}, \frac{A_{55}}{A_{11}}, \frac{B_{11}}{hA_{11}}, \frac{D_{11}}{h^2 A_{11}})$$

$$(\overline{I_0}, \overline{I_1}, \overline{I_2}) = (\frac{I_0}{I_0}, \frac{I_1}{hI_0}, \frac{I_2}{h^2 I_0})$$

$$\overline{N_{x0}} = \frac{N_{x0}}{A_{11}}$$

$$\tau = \frac{t}{L}\sqrt{\frac{I_0}{A_{11}}}$$

$$\omega = \Omega L\sqrt{\frac{I_0}{A_{11}}} \tag{11}$$

A_{11} and A_{55} are the elements of the stretching matrix. B_{11} *and* D_{11} are the elements of coupling and bending matrices respectively.

Finally, I_0, I_1, *and* I_2 are rotary, first and second inertia terms respectively. These terms are obtained as follows:

$$(A_{11}, B_{11}, D_{11}) = \int_{-h/2}^{h/2} Q_{11}(z)(1, z, z^2)dz$$

$$A_{55} = k_s \int_{-h/2}^{h/2} Q_{55}(z)dz$$

$$(I_0, I_1, I_2) = \int_{-h/2}^{h/2} \rho(z)(1, z, z^2)dz \tag{12}$$

k_s is a shear correction factor whose value is 5/6.

Different mechanical boundary conditions are used at the ends of the beam, which are clamped-clamped, hinged-hinged, and clamped-free. For clamped end $u,w, \psi=0,$ for hinged end $u,w=0, M_x=0$, for free end $M_x,=0, Q_x, N_x=0$

Non-dimensional parameters are as follows:

$$Clamped: u = w = \Psi = 0$$

$$Hinged: u = w = b_{11}\frac{\partial \overline{U}}{\partial \xi} + d_{11}\Psi = 0$$

$$Free: \begin{Bmatrix} a_{11}\dfrac{\partial \overline{U}}{\partial \xi} + b_{11}\dfrac{\partial \Psi}{\partial \xi} = 0 \\ \dfrac{\partial \overline{W}}{\partial \xi} + \eta\Psi = 0 \\ b_{11}\dfrac{\partial \overline{U}}{\partial \xi} + d_{11}\Psi = 0 \end{Bmatrix} \quad (13)$$

3. Solution of the Equations of Motion

Numerical approximation methods have many applications for partial differential equations solutions in various fields of engineering. Traditional methods such as finite difference and finite element methods are well known and their application has been developed. In these methods, the use of a large number of network points can lead to more accurate results, which requires the use of large-capacity computers. One of the effective methods for the numerical solution is the differential quadrature method (DQM). This method was first used by Bellman and Cassette in 1971 for solving partial differential equations [38]. The high accuracy of the results can be obtained by applying a small number of network points. Also, its simplicity has made it increasingly popular. Of course, this procedure also has disadvantages. As an example, we can point to the inefficiency of this method in the analysis of structures with loading, material properties, or discontinuous geometry. In the DQM method, the partial derivative of a function at a particular point is equal to the sum of the product of the weight coefficients of each point on the network in the value of the function of that point. Based on the DQM procedure, the derivative of a hypothetical point-like function is calculated as follows:

$$\frac{\partial^n f(x_i)}{\partial x^n} = \sum_{k=1}^{N_x} c_{ik}^{(n)} f(x_k), \quad i = 1,\ldots,N_x, \quad n = 1,\ldots,N_x - 1 \quad (14)$$

in Eq. (14), $c_{ik}^{(n)}$ are the weight coefficients.

The main point of this method is to calculate the weight coefficients and how to distribute the network points. Belman proposed two methods for calculating the weighting coefficients of a first-order derivative [38].

The first method is based on a set of algebraic equations. Unfortunately, when the number of network points is large, the matrix of this algebraic equation becomes bad. For this reason, this method is used for problems with a number of network points of 13 or less. The second method is to use Legendre polynomials of *N*-th degree that grid points are the roots of these polynomials. Therefore, the amplitudes of the grid points are fixed and the physics of the problem is not considered. This limits the DQ method in solving structural problems because in mechanical problems, various boundary conditions may appear and each boundary condition needs its own network points. Based on Belman's work, Shau and Richard introduced a method called the generalized differential quadrature method (GDQ), which overcame the previous method in obtaining weight coefficients of higher-order derivatives with an arbitrary distribution of lattice points [39]. In the GDQ method, the weighting coefficients of the first-order derivative are obtained as a simple algebraic relation using Lagrangian interpolation functions, as well as the weighting coefficients of the second-order and higher-order derivatives are calculated with a backslash expression according to the following equations [39].

$$c_{ij}^{(1)} = \frac{M^{(1)}(x_i)}{(x_i - x_j)M^{(1)}(x_i)}, \quad i, j = 1,2,\ldots,N, i \neq j$$

$$M^{(1)}(x_i) = \prod_{j=1, i\neq j}^{N} (x_i - x_j)$$

$$c_{ij}^{(n)} = n\left(c_{ii}^{(n-1)}c_{ij}^{(1)} - \frac{c_{ij}^{(n-1)}}{(x_i - x_j)}\right),$$

$$i, j = 1,2,\ldots,N_x, i \neq j, n = 2,3,\ldots,N_x - 1$$

$$c_{ii}^{(n)} = -\sum_{j=1, i\neq j}^{N} c_{ij}^{(n)}, \quad (15)$$

$$i = 1,2,\ldots,N_x, \quad n = 1,2,\ldots,N_x - 1$$

The selection of network points and how they are distributed plays a very effective role in achieving the convergence speed of the GDQ method. The non-uniform distribution of the network usually gives better results than its uniform distribution [40]. Bert and Malik showed that the distribution of network points varies according to the problem and suggested that for

structural mechanical problems, the Chebyshev-Gauss-Lobatto method be used to distribute network points in a one-dimensional network with points N_x in the interval [a, b] as follows [40]:

$$x_i = a + \frac{(b-a)}{2}\left(1-\cos\left(\frac{i-1}{N_x-1}\pi\right)\right), \quad i = 1, 2, ..., N_x \tag{16}$$

Applying GDQ expressed in Eqs.13-15 to the governing equations and related boundary conditions, will lead to a set of linear algebraic relations as follows:

$$\begin{aligned}
&a_{11}\sum_{k=1}^{N} c_{ik}^{(2)}\bar{U}(x_k) \\
&+\sum_{k=1}^{N} c_{ik}^{(1)}a_{11}(x_k)\sum_{k=1}^{N} c_{ik}^{(1)}\bar{U}(x_k) \\
&+b_{11}\sum_{k=1}^{N} c_{ik}^{(2)}\Psi(x_k) \\
&+\sum_{k=1}^{N} c_{ik}^{(1)}b_{11}(x_k)\sum_{k=1}^{N} c_{ik}^{(1)}\Psi(x_k) \\
&=\bar{I}_0\sum_{l=1}^{M} c_{fl}^{(2)}\bar{U}(\tau_l)+\bar{I}_1\sum_{l=1}^{M} c_{fl}^{(2)}\Psi(\tau_l) \\
&b_{11}\sum_{k=1}^{N} c_{ik}^{(2)}\bar{U}(x_k)+\sum_{k=1}^{N} c_{ik}^{(1)}b_{11}(x_k)\sum_{k=1}^{N} c_{ik}^{(1)}\bar{U}(x_k) \\
&+d_{11}\sum_{k=1}^{N} c_{ik}^{(2)}\Psi(x_k) \\
&+\sum_{k=1}^{N} c_{ik}^{(1)}d_{11}(x_k)\sum_{k=1}^{N} c_{ik}^{(1)}\Psi(x_k) \\
&-\eta a_{55}\left(\sum_{k=1}^{N} c_{ik}^{(1)}\bar{W}(x_k)+\eta\Psi(x_i)\right) \\
&=\bar{I}_1\sum_{l=1}^{M} c_{fl}^{(2)}\bar{U}(\tau_l)+\bar{I}_2\sum_{l=1}^{M} c_{fl}^{(2)}\Psi(\tau_l) \\
&a_{55}\sum_{k=1}^{N} c_{ik}^{(2)}\bar{W}(x_k) \\
&+\sum_{k=1}^{N} c_{ik}^{(1)}a_{55}(x_k)\sum_{k=1}^{N} c_{ik}^{(1)}\bar{W}(x_k) \\
&+\bar{N}_{x0}\sum_{k=1}^{N} c_{ik}^{(2)}\bar{W}(x_k) \\
&+\sum_{k=1}^{N} c_{ik}^{(1)}\bar{N}_{x0}(x_k)\sum_{k=1}^{N} c_{ik}^{(1)}\bar{W}(x_k) \\
&+\eta a_{55}\sum_{k=1}^{N} c_{ik}^{(1)}\Psi(x_k)+\eta\sum_{k=1}^{N} c_{ik}^{(1)}a_{55}(x_k)\Psi(x_i) \\
&=\bar{I}_0\sum_{l=1}^{M} c_{fl}^{(2)}\bar{W}(\tau_l)
\end{aligned} \tag{17}$$

$$\text{clamped}: \begin{Bmatrix} \bar{U}(x_i)=0 \\ \bar{W}(x_i)=0 \\ \Psi(x_i)=0 \end{Bmatrix}$$

$$\text{Hinged}: \begin{Bmatrix} \bar{U}(x_i)=0 \\ \bar{W}(x_i)=0 \\ b_{11}\sum_{k=1}^{N} c_{ik}^{(1)}\bar{U}(x_k)+d_{11}\Psi(x_i)=0 \end{Bmatrix} \tag{18}$$

$$\text{Free}: \begin{cases} a_{11}\sum_{k=1}^{N} c_{ik}^{(1)}\bar{U}(x_k)+b_{11}\sum_{k=1}^{N} c_{ik}^{(1)}\bar{U}(x_k)=0 \\ \sum_{k=1}^{N} c_{ik}^{(1)}\bar{W}(x_k)+\eta\Psi(x_i)=0 \\ b_{11}\sum_{k=1}^{N} c_{ik}^{(1)}\bar{U}(x_k)+d_{11}\Psi(x_i)=0 \end{cases}$$

where a_{ij} and b_{ij} are the first and second GDQ weighting coefficients respectively. Implementing the boundary conditions into Eq. 17 leads to the following algebraic system.

$$\begin{bmatrix}[S_{bb}] & [S_{bd}] \\ [S_{db}] & [S_{dd}]\end{bmatrix}\begin{Bmatrix}\{U_b\} \\ \{U_d\}\end{Bmatrix} - \overline{Nxo}\begin{bmatrix}[0] & [0] \\ [A_{db}] & [A_{dd}]\end{bmatrix} = \omega^2\begin{bmatrix}[0] & [0] \\ [0] & [\bar{I}_i]\end{bmatrix}\begin{Bmatrix}\{U_b\} \\ \{U_d\}\end{Bmatrix} \tag{19}$$

In Eq. (19), subscripts 'b' and 'd' refer to the points on the boundary and in the interior domain respectively. $\{U_b\}$ *and* $\{U_d\}$are the displacement component matrices of the points on the boundary and the interior domain respectively as follows:

$$\begin{aligned}\{U_b\} &= \{\{u_b\},\{w_b\},\{\psi_b\}\}^T \\ \{U_d\} &= \{\{u_d\},\{w_d\},\{\psi_d\}\}^T\end{aligned} \tag{20}$$

Eliminating the boundary degrees of freedom leads to the following equation:

$$([S]-\omega^2[\bar{I}])\{\overline{U_d}\} = 0 \tag{21}$$

The frequencies of the hybrid composite beams can be determined by solving the generalized eigenvalue problem Eq. (21). Clearly, the square of the lowest positive solution of Eq. (21) gives the frequency of beams. To investigate the buckling, we take ω =0 in Eq.(19) and we reach the following relation which is an eigenvalue problem.

$$([S]-\overline{Nxo}[A])\{\overline{U_d}\} = \{0\} \tag{22}$$

The non-dimensional frequency parameter as well as the buckling load are obtained by solving the eigenvalue problem as Eqs. (21-22). It is assumed $\Delta T(z) = T(z) - T_0$ and $T_0 = 0°\,C$.

4. Results and Discussion

4.1. Convergency and Validation Study

First of all, we present the convergence of the method. For this purpose, a hybrid composite beam with a CACA stacking sequence is considered. The beam is clamped at both ends. As noticed the convergency is fast and the dimensionless natural frequency converges at N=7.

Table 2. Convergence study (*L=165mm, h=1.3mm*)

N	$T_L=T_U=25^{oC}$	$T_L=25^{oC}$, $T_U=35^{oC}$
7	0.2215	0.2113
9	0.2216	0.2114
13	0.2216	0.2114
12	0.2216	0.2114
29	0.2216	0.2114
33	0.2216	0.2114

Now, we check the validity and efficiency of the GDQ method. Table 3 shows the non-dimensional natural frequency of an isotropic beam with clamped-clamped ends subjected to different uniform temperature rises $\mu_T = \Delta T \times 10^4$ and its comparison with similar results in Ref. [35]. As noticed there is good agreement between the results.

For further validation, the dimensionless natural frequency of a uniform FGM **(**functionally graded material**)** beam with clamped-clamped ends is compared with similar ones in Table 4.

Table 3. The non-dimensional natural frequency of an isotropic beam $\frac{L}{h}=\frac{50}{\sqrt{3}}, \upsilon = 0.3$

μ_T	0	1.2345	3.7037	7.4074
Present	23.3715	22.9217	22.153	20.4652
Ref.[35]	3.2370	2.8530	2.1393	20.9772
Error %	0.5	0.2	0.06	2

Table 4. The dimensionless natural frequency of an FGM beam for different *L/h*

	Present	Ref.[41]	Error %
$\frac{L}{h}=15$	0.02965	0.02893	2.5
$\frac{L}{h}=7$	0.12754	0.12836	0.6

4.2. Parametric Study

After checking the convergence and accuracy, we analyze the numerical results. First, the effect of the fiber hybrid ratio on thermal and mechanical properties is studied. The thermal properties of carbon and aramid fibers as reinforcement and epoxy resin as the matrix used in this study are presented in Table 5.

Table 6 Shows the influence of the hybrid ratio on the mechanical properties of the hybrid composite beam. As observed Young's modulus, shear's modulus, and thermal conductivity coefficient increase with increasing hybrid ratio because carbon fibers have a higher stiffness than aramid fibers. However thermal expansion coefficient decreases by increasing the hybrid ratio. The placement of carbon and aramid fibers will not affect the mechanical properties.

Table 5. Thermal properties of reinforcing fibers and epoxy resin

	carbon fiber (3K TORAY T300)	Aramid fiber (Kevlar 49)	Rezin epoxy (LY 5052-1)
Thermal expansion coefficient $\alpha \times 10^{-6}(1/^\circ C)$	-0.5	-2	71
Conductivity thermal coefficient $\mathrm{K}(w/m.k)$	14	0.31	0.15
Density $\rho(kg/m^3)$	1760	1440	1160
Young's modulus $E(Gpa)$	230	124	3
Shear's modulus $G(Gpa)$	96.25	47.75	2.96
Tensile strength MPa.	3530	3620	59.98

Table 6. Influence of the hybrid ratio on the mechanical properties of hybrid composite beam

Hybrid ratio	0%	29%	55%	79%	100%
$E(Gpa)$	44.64	58.14	71.63	85.10	98.61
$G(Gpa)$	18.36	24.34	30.31	36.26	42.25
$K(W/m.k)$	0.2048	1.649	3.093	4.51	5.96
$\alpha(1/^\circ C)$	45.85×10^{-6}	44.61×10^{-6}	43.36×10^{-6}	42.02×10^{-6}	40.88×10^{-6}

The effect of length-to-thickness ratio on dimensionless frequency for various end conditions is presented in Fig.3. This figure is for a composite hybrid beam type H4. As expected the dimensionless frequency decreases with the increase of this ratio.

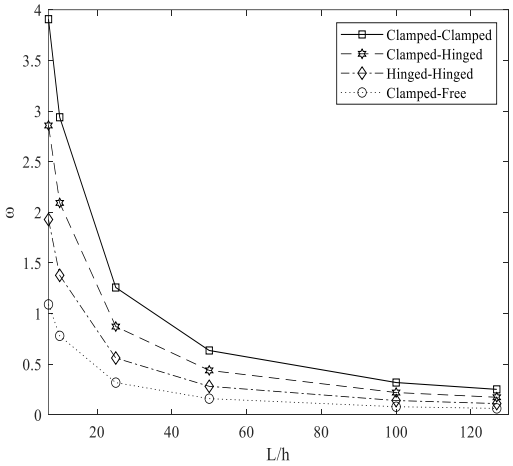

Fig. 3. Variations of the dimensionless natural frequency against length-to-thickness ratio

Table 7 Shows the influence of the fiber arrangement and hybrid ratio on the natural frequency. As observed the highest and least frequencies are related to the hybrid ratio of 100% (single composite reinforced with carbon fibers *CCCC*) and 0% (single composite reinforced with aramid fibers *AAAA*) respectively. That is because carbon fibers have higher stiffness than aramid fibers. Next, the highest frequencies are respectively related to the hybrid ratio 79% with the stacking sequence *CACC*, hybrid ratio 55% with stacking sequence *CAAC* and then *ACAC,* hybrid ratio 79% with stacking sequence *CCCA*, hybrid ratio 55% with stacking sequence *AACC*, hybrid ratio 29% with stacking sequence *CAAA,* hybrid ratio 55% with stacking sequence *ACCA* and finally hybrid ratio 29% with stacking sequence *ACAA.* The placement of the carbon fiber is very important.

The results show that the placement of carbon fibers on the upper and lower faces and the aramid fibers in the middle layers of the hybrid composite beam (*CAAC*) gives a higher frequency than the placement of these fibers in other modes. That is because the carbon fibers have a higher stiffness and the aramid fibers have higher toughness. On the contrary, when the aramid fibers are placed on the upper and lower surfaces like (*ACCA*), the toughness will be higher and more energy can be observed. In other words, for a hybrid ratio of 55%, a symmetrical stacking sequence with carbon fibers or aramid fibers on the upper and lower faces of the composite hybrid beam give the highest natural frequency as well as energy absorption respectively.

Table 7. Influence of fiber arrangement and hybrid ratio on the dimensionless natural frequency

Hybrid ratio (%)	Type	Stacking sequence	ω			
			C-C	C-H	H-H	C-F
0%	PFRP	*AAAA*	0.1879	0.1295	0.0829	0.0470
		CAAA	02141	0.1493	0.0926	0.0540
29%	HFRP	*ACAA*	01899	0.1309	0.0841	0.0475
55%	HFRP	*CAAC*	02508	0.1729	0.1107	0.0628
		ACAC	0.2216	0.1530	0.0986	0.0554
		AACC	.2157	0.1485	0.0980	0.0537
79%	HFRP	*ACCA*	0.1934	0.1333	0.0853	0.0484
		CACC	0.2509	0.1730	0.1109	0.0628
100%	CFRP	*CCCA*	0.2208	0.1526	0.0991	0.0553
		CCCC	0.2519	0.1736	0.1111	0.0630

The influence of thermal gradient on the non-dimensional natural frequency is presented for all types of hybrid composite beams in Fig. 4. It is concluded that the frequency has decreased with the increase of the temperature because the stiffness of the beam decreases with the increase of the temperature. This decrease in temperature will continue until the critical temperature of buckling is reached, and after that, the frequency will increase with the increase in temperature. The temperature at this point is the critical buckling temperature because the natural frequency of the beam at this point is very close to zero. As noticed the critical buckling temperature varies from 70 °K for *AAAA* to 140 °K for *CCCC*. For H1 type composite beam, this temperature increases from 78 °K to 138 °K with an increasing volume percentage of carbon fibers.

For the H2 type, the range of these changes is less and between 98 °K and 108 °K. From the comparison of two types of H1-*CACC* with H2-*ACCC*, both of which have a hybrid ratio of 79%, it is observed that the H1 has a greater critical temperature, and this shows that the way the fibers are placed is significant in hybrid composite beam design. Another interesting result that can be obtained from Figs. 4e-4f, which is related to H3 and H4 types, is that if the fibers are placed symmetrically relative to the middle axis of the beam, the critical temperature is almost the same.

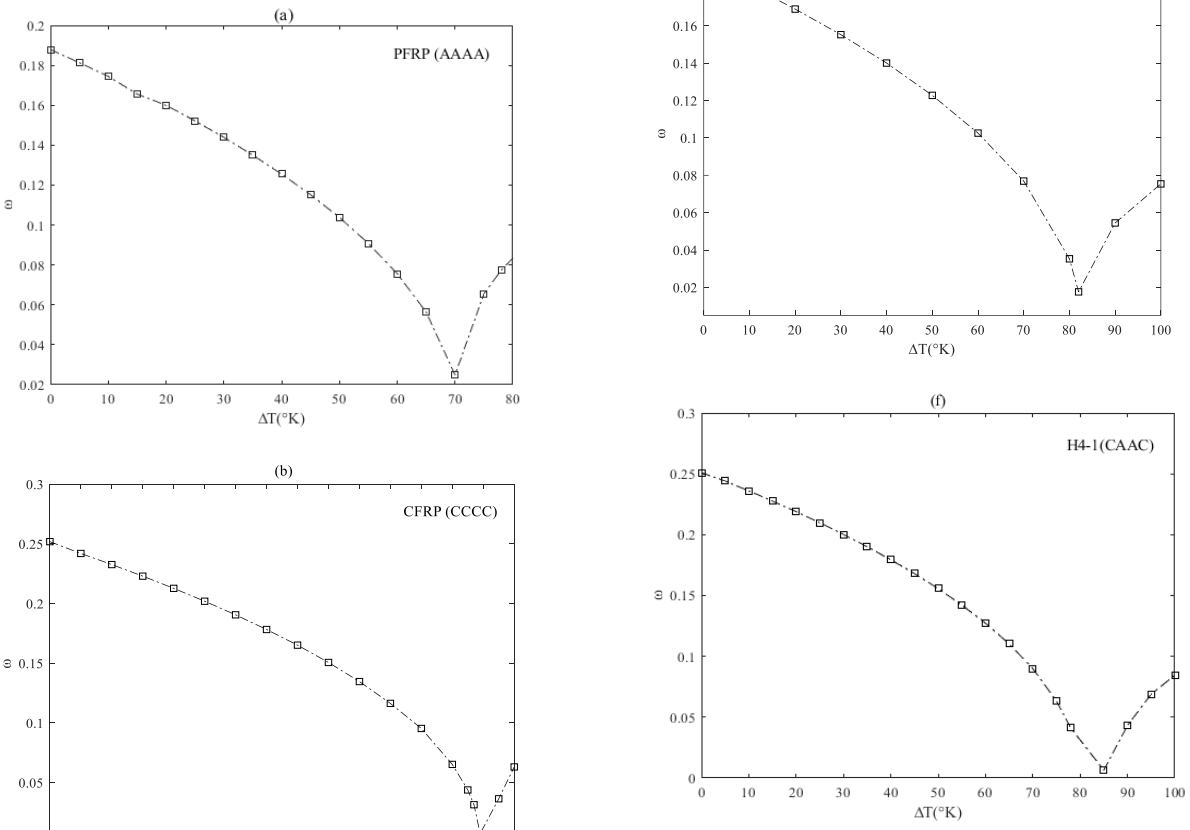

Fig. 4. Variations of the dimensionless natural frequency against ΔT for different types of hybrid composite beam

In the hybrid composites strengthened with both types of carbon fibers and aramid fibers in H1, and H2 arrangements, the buckling critical temperature as well as the buckling critical load increase with the increase of the hybrid ratio (increasing the volume fraction of carbon fibers).

Also, depending on the type of stacking sequence of the layers, in the case where the carbon fibers are on the outer layers (upper and lower layers of the beam), the critical temperature, as well as the buckling critical load, have a larger value, for example, in the hybrid ratio of 55%, comparing the two types of H3, H4 is observed that the buckling critical temperature and dimensionless buckling critical load of H4 is slightly greater than H3.

Figures 5-8 present the variations of the critical buckling load against the hybrid ratio for different H-type hybrid composite beams. As noticed in these figures, the critical buckling load increases with the increase of the number of carbon fibers and that is due to the greater strength of carbon fiber compared to aramid fiber. Similar to the dimensionless frequency, the placement of the fibers has an effect on the amount of the critical buckling load.

The interesting result from Figs 7-8 is that for types H3 and H4, where the fiber distribution is symmetrical with respect to the middle axis, unlike in Figs.4e-4f, where the critical buckling temperature was almost the same, here the critical buckling load is higher for type H4. As can be seen, the highest strength of a hybrid composite beam against buckling is related to the H1- type with stacking sequence as *CACC*.

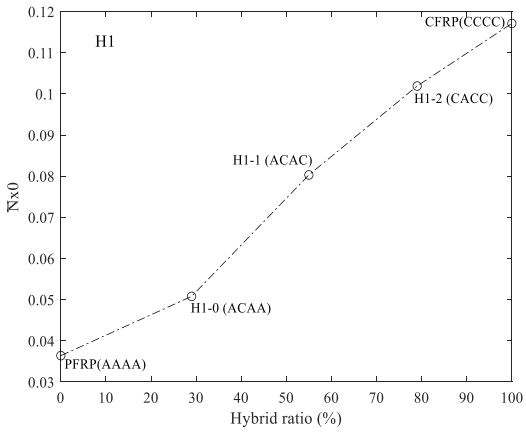

Fig. 5 Variations of critical buckling load against hybrid ratio for H1 type hybrid composite beam

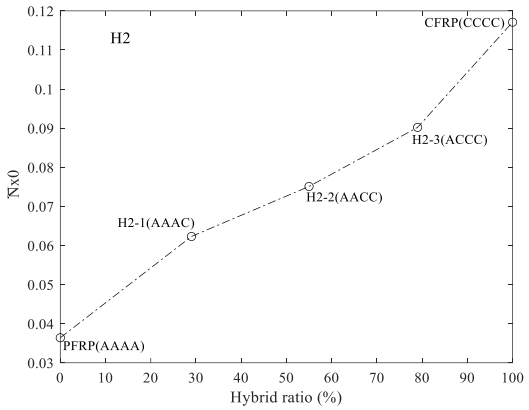

Fig. 6. Variations of critical buckling load against hybrid ratio for H2 type hybrid composite beam

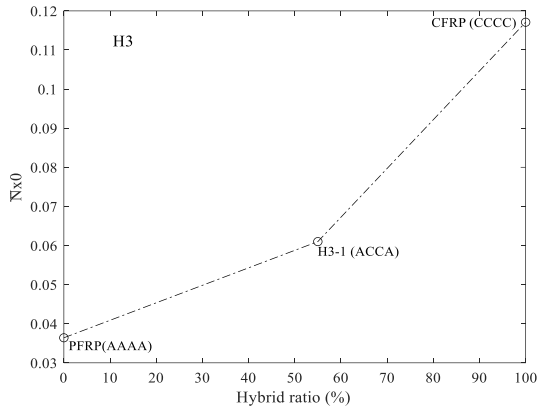

Fig. 7. Variations of critical buckling load against hybrid ratio for H3 type hybrid composite beam

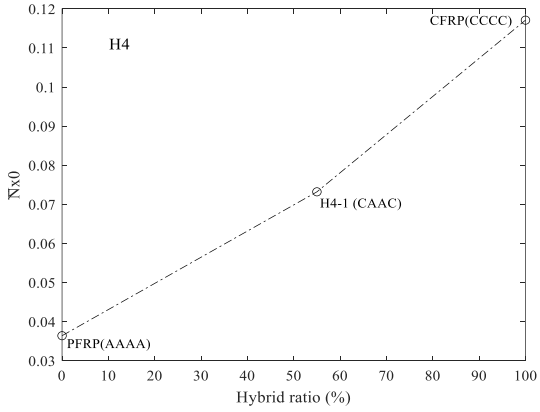

Fig. 8 Variations of critical buckling load against hybrid ratio for H4 type hybrid composite beam

Following the above figures, Table 8 shows the value of the dimensionless critical buckling load for different kinds of hybrid composite beams under various end conditions.

As expected, the largest critical buckling load occurs for a clamped-clamped hybrid composite beam.

Table 8. The dimensionless critical buckling load for different stacking sequence

Type		Stacking sequence	$\overline{Nx_0}$ Boundary conditions		
			C-C	C-H	H-H
PFRP		*AAAA*	0.0364	0.0187	0.0088
CFRP		*CCCC*	0.0732	0.0375	0.0178
H1	H1-0	*ACAA*	0.0508	0.0247	0.0120
	H1-1	*ACAC*	0.0803	0.0409	0.0200
	H1-2	*CACC*	0.1171	0.0598	0.0295
H2	H2-1	*AAAC*	0.0623	0.0324	0.0158
	H2-2	*AACC*	0.0751	0.0386	0.0200
	H2-3	*ACCC*	0.0902	0.0463	0.0227
H3	H3-1	*ACCA*	0.0610	0.0312	0.0148
H4	H4-1	*CAAC*	0.1019	0.0528	0.0252

Figs. 9(a-c) present the influence of the different fiber arrangement on the mode shapes. These figures show the first modes of vibrations for the case 1 (*ACAA, ACCA, CACC, CCCC)* and case2 (*AAAA, AACC, ACAC, AAAC, CAAC, ACCC)*, second mode for case 3 (*AAAA, AACC, CACC, CCCC)*, case 4 (*ACAA, ACAC, ACCA, AAAC, CAAC, ACCC)*, and third mode for case 5 (*AAAA, ACCA, AAAC, CAAC, CCCC)* and case 6 (*AACC, ACAA, ACAC, CACC, ACCC).*

The results show the second and third modes of H3 and H4 type (symmetrical stacking sequence) are the same, but their first mode is almost mirror to each other.

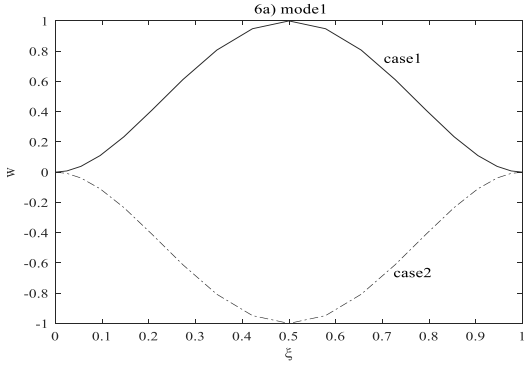

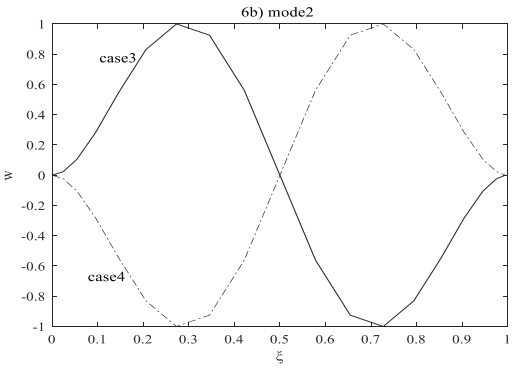

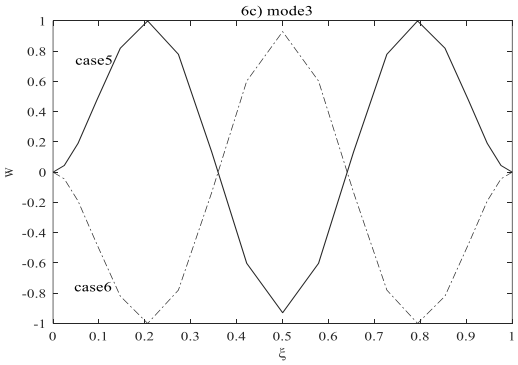

Fig 9. The shape of the first to three modes.

5. Conclusions

Theoretical free vibrations and buckling analysis of hybrid composite Timoshenko beam strengthened with the high strength carbon fibers/high toughness aramid fibers were studied under temperature gradient This is the first time that this kind of hybrid composite beam was analyzed for free vibration and thermal buckling under temperature gradient

The results show that the use of aramid fibers in the composite beam reinforced with carbon fibers decreases the natural frequency and the critical buckling load of the beam. It is also concluded that for types H3 and H4, where the fiber distribution is symmetrical with respect to the middle axis, the critical buckling temperature was almost the same, but the critical buckling load is higher for type H4. Also, the second and third modes of H3 and H4 type (symmetrical stacking sequence) are almost the same, but their first mode is almost mirror to each other.

As a result, the highest strength of a hybrid composite beam against buckling is related to the

H1- type with stacking sequence as *CACC*. Finally, this study can be a guide reference for the design and material selection of composite structures.

Compliance with Ethical Standards

On behalf of all authors, the corresponding author states that there is no conflict of interest.

Data availability

I confirm I have included data availability in my main manuscript file.

Nomenclature

P_H	Hybrid composite property
E	Young's modulus
G	Shear modulus
h	Thickness
I_0	Rotary inertia term
I_1	First inertia term
I_2	Second inertia term
K	Thermal conductivity coefficient
L	Length
M	Moment resultant
N	Force resultant
P_C	Carbon fiber properties
P_A	Aramid fiber properties
T	Temperature
u	*Axial displacement*
V_C	Volume percentage of carbon fiber
V_P	Volume percentage of aramid fiber
w	*Transverse displacement*
α	Thermal expansion coefficient
ρ	Density
ω	Natural frequency
Ψ	Rotation angle
ν	Poisson's ratio

References

[1] Ertekin, M., 2017. Aramid fibers, *Fiber technology for fiber-reinforced composites*, P.153-167.

[2] Sudarisman, Davies, IJ, Hamada H., 2007. Compressive failure of unidirectional hybrid fibre-reinforced epoxy composites containing carbon and silicon carbide fibres. *Compos. Part A*., 38: p.1070–1074.

[3] Nordin, H., Täljsten, B., 2004. Testing of hybrid FRP composite beams in bending. *Compos, Part B*, 35: p.2733.

[4] Bilisik, K., 2021. Aramid fiber reinforced composites, *Fiber reinforced composites*, p.515-559.

[5] Wang, Z., Li,H., Fei, B., Ashraf M., Xiong, Z., Lorenzo, R., Fang, C., 2021. Axial compressive performance of laminated bamboo column with aramid fiber reinforced polymer, *Composite Structures*, 258(15), 113398.

[6] Bazan, P., Nosal, P., Miernik, A.W., Kuciel, S., 2021. A novel hybrid composites based on biopolyamide 10.10 with basalt/aramid fibers: Mechanical and thermal investigation, *Composite Part-B,* 223(15), 109125.

[7] Al-Qureshi, HA., 2001. Automobile leaf springs from composite materials, *J. Mater Process Technol*, 01;118:5861.

[8] De la Rosa García, P., Escamilla, AC., 2013. Nieves González García, M., Bending reinforcement of timber eams with composite carbon fiber and basalt fiber materials. *Compos Part B Eng.,* 55: p.528–536.

[9] Mahdi, E., Hamouda, AMS., Sahari, BB., Khalid, YA., 2003. Effect of hybridisation on crushing behaviour of carbon/glass fibre/epoxy circular–cylindrical shells. *J Mater Process echnol.* 132: p.49–57.

[10] Zheng, N., Huang, Y., Liu, H-Y., Gao, J., Mai, Y-W., 2017. Improvement of interlaminar fracture toughness in carbon fiber/epoxy composites with carbon nanotubes/polysulfone interleaves. *Compos Sci Technol*.p.140:8–14015.

[11] Liu, B., Liu, Z., Wang, X., Zhang, G., Long, S., Yang, J., 2013. Interfacial shear strength of carbon fiber reinforced polyphenylene sulfide measured by the microbond test. *Polym Test*, 32: p.724–730.

[12] Taketa, I., Ustarroz, J., Gorbatikh, L., Lomov, SV., Verpoest, I., 2010. Interply hybrid composites with carbon fiber reinforced polypropylene and self-reinforced polypropylene. *Compos Part,* 41: p.927–932.

[13] Paiva, JMF. De., Santos, AND. Dos., Rezende, MC., 2009. Mechanical and morphological characterizations of carbon fiber fabric reinforced epoxy composites used in aeronautical field. *Mater Res,* 12: p.367–374.

[14] Hassani, F., Martin, PJ., Falzon, BG., 2020. Progressive failure in interply hybrid composites of self-reinforced polypropylene and glass fibre. *Polymer,* 195:122411.

[15] Zhang, J., Duan, Y., Wang, B., Zhang, X.,2020. Interfacial enhancement for carbon fibre reinforced electron beam cured polymer composite by microwave irradiation. *Polymer,* 192:122327.

[16] Park, R., Jang, J., 1999. Performance improvement of carbon fiber/polyethylene fiber hybrid composites. *J Mater Sci*, 34: 2903–10.

[17] Hwang, S-F., Mao, C-P.,1999. The delamination buckling of single-fibre system and interply hybrid omposites. *Compos Struct,* 46:279–287.

[18] Subagia ID., Kim Y, Tijing LD, Kim CS, Shon HK., 2014. Effect of stacking sequence on the

flexural properties of hybrid composites reinforced with carbon and basalt fibers. *Compos Part B Eng*, 58:2518.

[19] Nisini, E., Santulli, C., Ceruti, A., Liverani A., 2018. High speed impact properties of carbon-basalt-flax DHEC composites compared with pure carbon fibre composites. *Compos Struct,* 192: p.165–172.

[20] Yang, K., Guan, J., Numata, K., Wu, C., Wu, S., Shao, Z., et al., 2019. Integrating tough Antheraea pernyi silk and strong carbon fibres for impact-critical structural composites. *Nat commun*, 10: 1-12

[21] Subagia, IDGA, Kim Y. 2013. Tensile behavior of hybrid epoxy composite laminate containing carbon and basalt fibers. *Sci Eng Compos Mater*, 21: p.211–217.

[22] Li, Y., Xian, XJ., Choy, CL., Guo, M., Zhang, Z., 1999. Compressive and flexural behavior of ultra-high-modulus polyethylene fiber and carbon fiber hybrid composites. *Compos Sci Technol,* 59: p.13–18.

[23] Chang, J, Niu H, Zhang M, Ge Q, Li Y, Wu D., 2015. Structures and properties of polyimide fibers containing ether units, *J Mater Sci* 50: p.4104–4014.

[24] Wu, D., Chang, J., Ge, Q., Zhang, M., Liu, W., Cao, L., 2015. Effect of pre-imidization on the structures and properties of polyimide fibers. *RSC Adv*, 85.

[25] Zhang, M., Niu, H., Wu, D., 2018. Polyimide Fibers with High Strength and High Modulus: Preparation, Structures, Properties, and Applications, *Macromol Rapid Commun*, 39, 1800141.

[26] Li, S., Zhuo, H., Han, E., Zhang, D., Liu, G., Tian, G., 2020. Preparation and properties of high strength and high modulus polyimide fiber/modified cyanate resin composites, *Acta Mater Compos Sin*, 37: p.42–49.

[27] Zhuo, H., Li, S., Han, E., Zhang, D., Liu, G., Tian, G., 2019. Mechanical properties and failure mechanism of high strength and high modulus polyimide fiber reinforced epoxy composites, *Acta Mater Compos Sin,* 36: p.2101–2109,

[28] Cheon J., Lee,M., Kim, M., 2020. Study on the stab resistance mechanism and performance of the carbon, glass and aramid fiber reinforced polymer and hybrid composites, *Composite Structures*, 234(15), 111690,

[29] Enew,M.A., Abd Elfattah, M.,Fouda,S.R., Hawash,S.A., 2021. Effect of aramid and carbon fibers with nano carbon particles on the mechanical properties of RPDM rubber thermal insulators for solid rocket motors applications, *Polymer testing*,103,107341.

[30] Kim,S., Lee,J., Roh, C., Eun, J., Kang, C., 2019. Evalulation of carbon fiber and p-aramid composite for industrial helmet using cross-ply for protecting human heads, *Mechanics of Materials*, 139, 103203.

[31] Farrokhian A., Salmani-Tehrani M.,2020. Surface and small scale effects on the dynamic buckling of carbon nanotubes with smart layers assuming structural damping, *Steel and Composite Structures,*37(2), p.229-251.

[32] Farrokhian A., 2020. The effect of voltage and nanoparticles on the vibration of sandwich nanocomposite smart plates, *Steel and Composite Structures*,34(5), p.733-742.

[33] Soltani M., Abolghasemian R., Ghasemi A.R., Shafieirad M., Abbasi Z., Amiri-Mehra A.H., 2023. Laminated optimization of non-uniform I-shaped beams under transversely loading with clamped-free boundary conditions, *Structures*, 47, p. 1524-1530.

[34] Soltani A., Soltani M., 2022. comparative study on the lateral stability and strength of laminated composite and fiber metal laminated I-shaped cross section beams, *J. Computational Applied Mechanics,* 53(2), p.190-203.

[35] Soltani M., Abolghasemian R., Ghasemi A.R., 2022. Multi-objective optimization of lateral stability strength of transversely loaded laminated composite beams with varying I-section, *J. Composite Materials,* 56(12).

[36] Soltani M., 2022. A Novel approach for lateral buckling assessment of double tapered thin-walled laminated composite I-beams, *Mechanics of Advanced Composite Structures*, 9(1), p.11-23.

[37] Aydin, M., Acar, V., Cakir, F., Gundogdu, O., Akbulut, H., 2022. Comparative dynamic analysis of carbon, aramid and glass fiber reinforced interply and intraply hybrid composites, *Composite Structures*, 291, 115595.

[38] Bellman, R., Cassette, J., 1971. Differential quadrature and long-term integration, *J. of Mathematical Analysis and Applications*, 34(2), p.235-238.

[39] Shu, C., Richards, B.E., 1992. Application of generalized differential quadrature to solve two-dimensional incompressible Navier-Stokes equations, Int. *J. for Numerical Methods in Fluids,* 15(7)., p.791-798.

[40] Bert, C.W., Malik, M., 1996. Differential quadrature method in computational mechanics: a review, *Applied Mechanics Reviews,* 49, p.1-28.

[41] Xiang, H.J., Yang, J., 2008. Free and forced vibration of a laminated FGM Timoshenko beam of variable thickness under heat conduction, *Composites: Part B,* 39, p. 292–303.